Ocean Engineering 347 (2026) 123975

Contents lists available at ScienceDirect

Ocean Engineering

journal homepage: www.elsevier.com/locate/oceaneng

Research paper

A hybrid model framework for wave attenuation by flexible vegetation in current-wave flows

Weifeng Ye [a], Zhan Hu [a,b,c,d,*], Khanh Linh Phan [e], Marcel Stive [f]

[a] School of Marine Sciences, Sun Yat-Sen University and Southern Marine Science and Engineering Guangdong Laboratory (Zhuhai), Zhuhai, 519082, China
[b] Guangdong Provincial Key Laboratory of Marine Resources and Coastal Engineering, Guangzhou, 510006, China
[c] Pearl River Estuary Marine Ecosystem Research Station, Ministry of Education, Zhuhai, 519082, China
[d] Guangdong Pearl River Estuary National Integrated Monitoring Station for Ecological Quality of Marine Ecosystem, Zhuhai, Guangdong, 519070, China
[e] Hydraulic Department, Faculty of Civil Engineering, Thuy Loi University, Viet Nam
[f] Hydraulic Department, Faculty of Civil Engineering and Geosciences, Delft University of Technology, the Netherlands

ARTICLE INFO

Keywords:
Flexible vegetation
Wave attenuation
Wave-induced vertical velocity
Semi-analytical model
Hybrid framework

ABSTRACT

Salt marsh wetlands can serve as an efficient buffer against storm waves. However, accurate quantification of the wave attenuation process is challenging. Previous modeling approaches generally ignored the posture of flexible vegetation and the impact of wave-induced vertical velocity, which may lead to underestimated wave attenuation. To address this issue, we developed a new hybrid model framework for wave attenuation by flexible vegetation. This framework incorporates a machine learning predictor for vegetation posture via a bending coefficient and a modified semi-analytical model that accounts for wave attenuation by bent rigid vegetation. This model framework is compared with our own experimental data and additional data from literature. The model shows that flexible vegetation can induce up to 21 % greater wave attenuation than rigid vegetation in near-emergent testing conditions due to the contribution of wave-induced vertical velocity. Our model framework can accurately reproduce such a contribution (up to 60 % of the total wave energy), and avoid underestimation of attenuation ($R^2 = 0.96$). This study develops a novel tool integrating mechanical analysis and data-driven approaches to quantify wave attenuation by flexible vegetation, enabling the assessment of coastal protection by salt marshes and seagrass wetlands.

1. Introduction

Coastal regions are increasingly threatened by natural disasters, including storm waves and erosion. While traditional gray infrastructures, such as seawalls and breakwaters, provide hard protection, they are often expensive and environmentally harmful (Morris et al., 2018; Daro Justine and Seenath, 2025). Alternatively, nature-based solutions that incorporate mangroves, salt marshes, and seagrass as buffers of coastal protection, not only mitigate flood risks but also offer ecosystem services like wastewater purification and carbon storage (Barbier et al., 2011; Temmerman et al., 2023). A recent study on a marsh-fronted seawall demonstrated benefit-cost ratios exceeding one in various scenarios, highlighting their economic feasibility (Lee and Nepf, 2024). Accurate assessment of the wave attenuation by vegetation is essential for these benefit-cost ratio analyses and justification of applying nature-based solutions for coastal protection.

The methodologies for simulating wave attenuation by rigid vegetation under pure wave conditions are well-developed (Dalrymple et al., 1984; Mendez and Losada, 2004). In contrast, wave attenuation by flexible vegetation is more complex due to stem bending and swaying with the water flow (Leclercq and de Langre, 2018). To address this, researchers have employed methods such as large-eddy simulation and smoothed particle hydrodynamics (Wang et al., 2022; El Rahi et al., 2023). While this approach offers a detailed simulation of the wave attenuation process, it is computationally very expensive to sustain wide applications in engineering projects.

As an alternative to expensive numerical modeling, previous studies have employed rigid vegetation models for wave attenuation assessment (Table 1). To account for the effects of flexible vegetation, the Modified Drag Coefficient method incorporates modified (typically reduced) drag

* Corresponding author. School of Marine Sciences, Sun Yat-Sen University and Southern Marine Science and Engineering Guangdong Laboratory (Zhuhai), Zhuhai, 519082, China.
E-mail address: huzh9@mail.sysu.edu.cn (Z. Hu).

https://doi.org/10.1016/j.oceaneng.2025.123975
Received 29 May 2025; Received in revised form 29 November 2025; Accepted 10 December 2025
Available online 23 December 2025

coefficients into a rigid vegetation model (Anderson and Smith, 2014; Losada et al., 2016). However, this method tends to aggregate the various factors, such as vegetation flexibility and hydrodynamics in the modified drag coefficients, making it difficult to distinguish individual contributions and key driving processes. Consequently, this limitation impedes a more detailed analysis of the wave attenuation process, and the accuracy of this simulation method depends on how well the drag coefficient is fitted.

The Effective Length method is a notable contribution that provides a comprehensive theoretical framework considering wave attenuation process by flexible vegetation in pure wave and combined current-wave flow (Zhang and Nepf, 2021; Schaefer and Nepf, 2022). It simplifies the complex vegetation-wave interaction by converting the dynamics of vegetation into an equivalent rigid vegetation model with similar force characteristics. Empirical formulas facilitate its application, and its validity has been demonstrated by its application (Zhu et al., 2022; Vettori et al., 2024). Additionally, Vettori et al. (2025) presented an analytical model focusing on turbulence-enhanced wave attenuation induced by the shear layer at the canopy top. However, the Effective Length method primarily considers horizontal velocity components in wave energy attenuation. This may lead to an incomplete representation of the vertical forces induced by waves, which could contribute significantly to wave attenuation.

The Hydraulic Standing Biomass (HSB) method is a new approach for estimating wave attenuation using a novel variable HSB, which depends on average vegetation height, dry weight, water depth, and incoming wave conditions (Maza et al., 2022; Lopez-Arias et al., 2023). This method establishes a linear relationship between HSB and wave height attenuation, thereby eliminating the need for calibration-dependent coefficients, such as drag coefficients. However, since the method is derived from experimental data fitting, it may be limited to scenarios like those experimental conditions. Additionally, due to its parameter settings, the method may not be applied in wave-current interaction conditions.

The methods outlined above offer practical solutions with differing levels of simplification. Although these methods provide computational benefits, they often ignore the potential contribution of wave-induced vertical flow velocities, which may lead to underestimation of the wave energy attenuation.

This study aims to develop a new modeling framework for wave attenuation by flexible vegetation in combined wave-current flows, explicitly considering the bending of vegetation and the contribution of vertical flow velocities to energy attenuation. This framework is computationally inexpensive and can facilitate the quantitative analysis of various factors influencing wave attenuation. This framework has a hybrid structure that combines a machine learning predictor for vegetation deflection, and a semi-analytical model that accounts for the wave attenuation by the bent vegetation. The contribution of both horizontal and vertical velocity is included. The model is tested against our own experimental data and data from previous experiments. The model performance and the insights generated by the modeling framework are included in the following sections.

2. Methods

2.1. Experimental setup and test conditions

Laboratory experiments were conducted in a wave-current flume at the Hydrodynamics Laboratory of Sun Yat-sen University, China (Fig. 1a). The flume is 26 m in length, 0.6 m in width and 0.6 m in height. Regular waves were generated by a piston-type wavemaker installed at the left end of the flume. The tailgate can be adjusted to regulate the water level and, in conjunction with water pumps, control the flow velocity. Although the current near the wavemaker is initially perpendicular to the direction of wave propagation, it becomes vertically uniform before reaching the vegetation zone.

A ramp-type wave absorber was installed near the tailgate to minimize wave reflection. In pure wave or opposing current scenarios, the tailgate height was adjusted to align with the still water level, allowing partial wave overtopping into the reservoir. For following current scenarios, the tailgate was positioned below the still water level, enabling most waves to propagate directly into the reservoir. Under near-emergent conditions, wave height attenuation was substantial, eliminating the need to consider wave reflection. To prevent complex wave reflection effects, the wavemaker was deactivated after approximately 30 waves in each test.

Cylindrical flexible mimic canopies were arranged in a staggered pattern. The canopy fully covered the width of the flume and extended continuously over a length of 6 m. The flexible vegetation (Fig. 1b), constructed from silicone foams (ρ = 741 kg/m^3), was mounted on a false bottom with a height of 17 cm. Each stem measured 25 cm in height and 1 cm in diameter, with a flexural rigidity EI of $2.95 \pm 0.15 \times 10^{-4}$ (mean $\pm$ standard deviation, measured using tensile testing under the assumption of material isotropy).

Six force sensors (UTILCELL Model 140) were installed at three positions (x = 1, 3, and 5 m) to synchronously measure forces on flexible and rigid vegetation mimics. At each position, two sensors were mounted, operating at a frequency of 50 Hz, to measure force on a stainless steel rod (representing rigid vegetation) and a silicone foam rod (representing flexible vegetation), respectively (Fig. 1c). To prevent collisions between flexible vegetation mimics and the sensors during the experiments, some mimics near the sensors were partially removed (Fig. B1). The sensors, enclosed in aluminum protective casings, were securely mounted inside the false base. These sensors have a nominal capacity of 3 kg, a minimum division of 0.3 g, and a total error (nonlinearity and hysteresis) of less than ±0.017 % of the nominal sensitivity, as per the manufacturer's datasheet. The force measurements can be decomposed into the following form:

$$F(t) = F_{mean} + F_w \sin \omega t + F' \tag{1}$$

where F_{mean} is the mean value of the force, F_w is the amplitude of force fluctuation, ω is the angular frequency of fluctuation determined by the wave period T and t is time. F' is the random perturbation term, which is ignored in data processing because it is not a dominant factor in wave attenuation. According to the root mean square method, F_w can be derived from the force time series recorded during the steady-state phase

Table 1
A review of quantification methods for wave attenuation by flexible vegetation.

Methods	Drag coefficient	Wave-current interaction	Predictive tool	Vertical force	Vegetation schematization
Modified Drag Coefficient method (Anderson and Smith, 2014; Losada et al., 2016)	Modified considering flexibility	Yes	Drag coefficient formula	No	Rigid and vertical rods
Effective Length method (Zhang and Nepf, 2021; Schaefer and Nepf, 2022)	Origin	Yes	Effective Length formula	No	Rigid and vertical rods
Hydraulic Standing Biomass method (Maza et al., 2022; Lopez-Arias et al., 2023)	None	No	HSB formula	No	HSB
Hybrid model (Present study)	Origin	Yes	XGBoost predictor	Yes	Rigid and bent rods

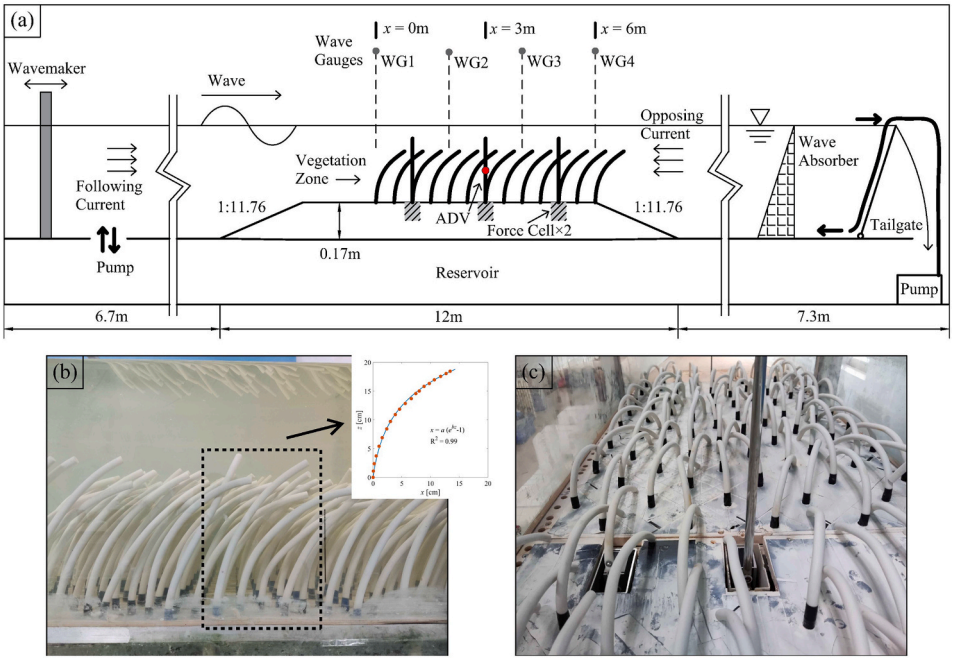

Fig. 1. (a) Schematic of the flume experimental set-up (not to scale), adapted from Ye and Hu (2023). (b) Artificial flexible vegetation submerged in water, with a vegetation density of 556 stems/m^2. (c) Synchronized measurement of forces on both flexible and rigid rod.

of the waves (Lei and Nepf, 2019b; Zhang and Nepf, 2021):

$$F_w = \sqrt{\frac{2}{NT}\int_0^{NT} (F(t) - F_{mean})^2 dt} \tag{2}$$

where N is the number of wave periods in the selected time series. The time series processing in this study requires the selection of at least 16 wave periods.

The wave attenuation over a meadow was measured using four capacitive wave height gauges (WG1-4) at a frequency of 50 Hz. Wave height is obtained as:

$$H = 2\sqrt{\frac{2}{NT}\int_0^{NT} (\eta(t) - \eta_{mean})^2 dt} \tag{3}$$

where η_{mean} refers to the mean value of the surface elevation. The relative wave height, denoted as:

$$H_r = H(x)/H_0 \tag{4}$$

where H_0 representing the incident wave height at $x = 0$. During the experiment, wave height data were collected using four wave gauges positioned at $x = 0$, 2, 4, and 6 m within the vegetation fields. Control experiments, conducted in the absence of vegetation, were used to adjust the wave height attenuation results and eliminate the influence of external factors such as friction (Augustin et al., 2009; Reis et al., 2024).

The wave attenuation capability of vegetation patch with a length of L_v is evaluated by 1 - K_t, where K_t is the transmission coefficient. The expression for K_t is:

$$K_t = H_r(x = L_v) \tag{5}$$

During the experiment, velocity was measured at half the vegetation deflected height using a Nortek Vectrino (ADV) at a sampling rate of 50 Hz, with an accuracy of ±0.5 %. ADV data were recorded only when the signal-to-noise ratio exceeded 15 dB and the correlation was greater than 80 %. The velocity time series can also be expressed as (Van Veelen et al., 2025):

$$U(t) = U_{mean} + U_w \sin \omega t + U' \tag{6}$$

where U_{mean} represents the mean velocity during the wave event, and U_w represents the wave orbital velocity, which can be obtained by applying the root mean square method. U' is the turbulence perturbation term, which is ignored in data processing. In this study, $|U_{mean}| + U_w$ is used as the characteristic velocity.

The experiments were conducted on a vegetation canopy subjected to regular waves under various conditions, including wave height (3–5 cm), wave period (0.6–1.0 s), water depth (20–33 cm), and imposed current velocity (U_0, −12–15 cm/s). Two vegetation densities were tested: namely high density (556 stems/m^2) and low density (139 stems/m^2). A total of 180 experimental cases combining regular waves and currents were conducted (Table 2). In these experiment, the deflected height in water was 20 cm. Thus, the condition with a water depth of 20 cm in Table 2 corresponds to a near-emergent state. To enhance the reliability of the results, each test was repeated three times. Additionally, scenarios involving wave breaking were omitted to focus on the analysis of the drag force effect.

Table 2
Experimental conditions for flexible vegetation in combined wave-current.

Water depth (h) [cm]	Vegetation density (N_v) [stems/m^2]	Wave height (H_0) [cm]	Wave period (T) [s]	Wave case name	Current velocity (U_0) [cm/s]
20	139/556	3	0.6	Wave0306	0/±3/±6/±9/±12[a]
		3	0.8	Wave0308	
		5	0.6	Wave0506	
		5	0.8	Wave0508	
		5	1.0	Wave0510	
33	139/556	5	0.6	Wave0506	0/±3/±6/±9/+12/+15
		5	0.8	Wave0508	
		5	1.0	Wave0510	
		7	0.8	Wave0708	
		7	1.0	Wave0710	

[a] The ± symbol indicates that experiments were conducted under both following and opposing current conditions.

2.2. Hybrid model for wave attenuation by flexible vegetation

The hybrid model integrates a machine learning predictor and a semi-analytical model. The semi-analytical model was adapted from an existing model to simulate wave height attenuation induced by vertical rigid vegetation in combined wave-current flow (Ye and Hu, 2023). A rectangular coordinate system is defined in Fig. 2a, with the leading edge of the vegetation zone located at $x = 0$ and the still water level at $z = 0$, and waves propagating in the positive x-direction. Before entering the vegetation zone, the current is uniform across the water depth with a velocity of U_0.

This model is based on the following assumptions:

1. Linear wave theory is valid;
2. The current velocities within and above the canopy are vertically uniform, denoted as U_{in} and U_{up}, respectively;
3. The current and waves are collinear;
4. The drag coefficient is constant within the canopy;
5. Flexible vegetation is conceptualized as rigid but bent cylinders (Fig. 2b);
6. The circular frequency remains constant both before and during the propagation of waves through the canopy.

This study applies the wave energy flux balance equation:

$$\frac{\partial}{\partial x}\left[E\left(C_g + U_0\right) + S_x U_0\right] = -\varepsilon_{wc\_w} \tag{7}$$

where $E = \rho g H^2/8$ is the wave energy per horizontal area, ρ is the density of water, g is the gravitational acceleration, H is the wave height, S_x is the radiation stress and C_g is the relative group velocity. Although Eq. (7) is formulated for a vertically uniform current, it is applied here to a two-layer flow system. In this application, the depth-averaged current velocity U_0 is still employed as a part of the group velocity. This serves as a pragmatic simplification to parameterize the wave-current interaction within the two-layer flow system. Wave energy propagates at the group velocity $C_g + U_0$, which can be mathematically expressed as:

$$C_g + U_0 = \frac{\sigma_{wc}}{2k}\left(1 + \frac{2kh}{\sinh 2\,kh}\right) + U_0 \tag{8}$$

Here, k represents the wave number, h is the water depth and σ_{wc} denotes the relative circular frequency, which satisfies the following dispersion relation:

$$\sigma_{wc} = \sigma - U_0 k = \sqrt{gk\tanh(kh)} \tag{9}$$

where $\sigma = 2\pi/T$ is circular frequency which is related to the wave period T.

In a wave-current field, the time-averaged flow structure alters the wave dispersion relationship through the Doppler shift effect. Although models exist for idealized shear flows (Chen and Zou, 2019), they are not directly applicable to the flow profiles encountered here. Given that our study uses a uniform two-layer flow approximation, we therefore adopt the simpler dispersion relationship for a uniform one-layer flow. In this study, the horizontal flow field is expressed as:

$$U = \begin{cases} U_{up} + \dfrac{\sigma_{wc} H}{2}\dfrac{\cosh k(h+z)}{\sinh kh}\cos(kx - \sigma t), & (-h + h_d < z < \eta) \\ U_{in} + \dfrac{\sigma_{wc} H}{2}\dfrac{\cosh k(h+z)}{\sinh kh}\cos(kx - \sigma t), & (-h < z < -h + h_d) \end{cases} \tag{10}$$

where h_d. is the deflected height and η is the free surface of water. The total length of the vegetation stem is denoted by h_v. This study adopts the method proposed by Chen et al. (2013) to predict the uniform two-layer flow, with further details provided in Ye and Hu (2023), which are not reiterated here. The horizontal flow velocity structure for flexible vegetation experiments in this study can be found in Appendix A.

Aquatic plants are susceptible to bending and, in some cases, flattening (Fig. 2c–d). The Effective Length method models flexible

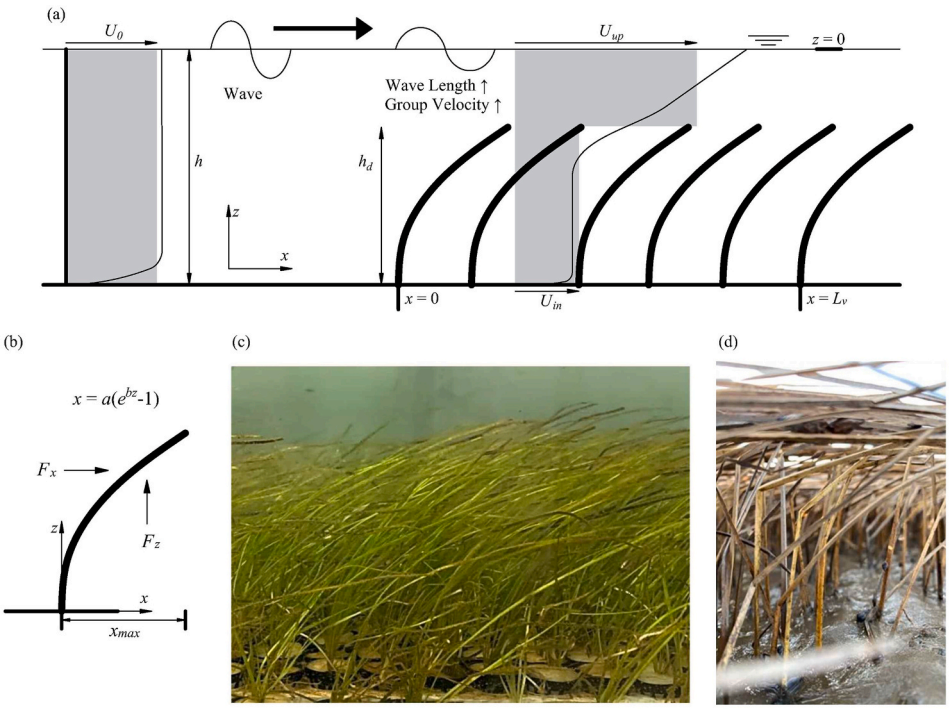

Fig. 2. (a) Schematization of wave-current-vegetation interaction, adapted from Ye and Hu (2023). The depth-uniform current U_0 is transitions into a two-layer distribution within the vegetated area, with internal velocity U_{in} below the deflected vegetation height h_d and upper velocity U_{up} above it. (b) Both horizontal force F_x and vertical force F_z act on the bent vegetation. (c) Morphology of *Vallisneria nana* in flow (Adapted from Li et al., 2024). (d) Flattened *S. mariqueter* (Adapted from Ma et al., 2023).

vegetation as rigid, vertical vegetation under identical force conditions (Luhar and Nepf, 2016; Schaefer and Nepf, 2022). In contrast, this study presents an alternative approach, modeling flexible vegetation as rigid, bent vegetation with equivalent wave attenuation (Fig. 2b). In this context, the vertical velocity within the flow field also contributes to the work done, which can be expressed as:

$$W = \frac{\sigma_{wc} H}{2} \frac{\sinh k(h+z)}{\sinh kh} \sin(kx - \sigma t) \tag{11}$$

The bending posture of the flexible mimics observed in the experiments (Figs. 1b and 2b) was digitized and analyzed. To mathematically represent its shape, several candidate functions were evaluated. The expression given in Eq. (12) was ultimately selected as it provided the best empirical fit in terms of the coefficient of determination (R^2).

$$x = a\left(e^{bz} - 1\right) \tag{12}$$

This relationship ensures that the stem intersects at the origin (0, 0). For other vegetation forms, such as flattened vegetation, alternative relationships may be employed. The projection length of the bent stem on the x-axis is denoted as $x_{\max}$, where $x_{\max}$ does not exceed the total vegetation height h_v.

To examine the individual effects of coefficients a and b on wave attenuation, we conducted a parameter sensitivity analysis using the model mentioned above (Fig. 3). Based on the realistic morphology of the vegetation, the initial parameter values were set as $a_0 = 0.0095$ and $b_0 = 10$. In these idealized experiments, we varied one coefficient (e.g. a) while holding the other constant at its initial value (e.g. $b = b_0$). All other conditions, including the incident wave ($H_0 = 5$ cm, $T = 0.8$ s), water depth ($h = 20$ cm), and vegetation properties ($h_v = 25$ cm, $N_v = 556$ stems/m^2), were kept unchanged. The results indicate that the residual wave height exhibits a consistent trend for both parameters a and b: it initially decreases and then increases. However, coefficient b demonstrates significantly greater sensitivity compared to coefficient a. To simplify the expression of vegetation bending for easier variable control, coefficient a can be treated as a constant (e.g. 0.0095), while coefficient b is the bending coefficient depicting the degree of vegetation bending.

Eq. (12) can also be treated in a conceptual form of vegetation deflection that corresponds to wave attenuation capability, and the bending coefficient b can be calibrated through experimental results.

The total energy decay rate in our model comprises three components: $\varepsilon_{cw,x}$ is the total horizontal dissipation under wave-current interaction, $\varepsilon_{cw\_c,x}$ is the pure current induced dissipation, and $\varepsilon_{cw,z}$ is the vertical velocity induced dissipation. Since $\varepsilon_{cw\_c,x}$ only modifies the potential energy of the free surface, it should be excluded from the wave energy dissipation term (Hu et al., 2014; Ye and Hu, 2023).

$$\begin{aligned}
\varepsilon_{cw,x} &= \frac{1}{2}\rho N_v C_D b_v \left\langle \int_{-h}^{-h+h_d} U^2 |U| dz \right\rangle \\
\varepsilon_{cw_c,x} &= \frac{1}{2}\rho N_v C_D b_v \left\langle \int_{-h}^{-h+h_d} U_{in}^2 |U_{in}| dz \right\rangle \\
\varepsilon_{cw,z} &= \frac{1}{2}\rho N_v C_D b_v \left\langle \int_{0}^{x_{\max}} W^2 |W| dx \right\rangle \\
\varepsilon_{cw_w} &= \varepsilon_{cw,x} - \varepsilon_{cw_c,x} + \varepsilon_{cw,z}
\end{aligned} \tag{13}$$

where N_v is the vegetation density, C_D is the drag coefficient, b_v is the stem diameter, and $< >$ denotes wave-period averaging. The parameters $x_{\max}$ and h_d, which govern the wave attenuation process, are determined by the bending coefficient. In this study, C_D for rigid vegetation is applied to the flexible case (Eqs. (15)–(17) in Ye and Hu, 2023). The C_D formula is a function of the Reynolds number, which is defined based on the stem diameter as the characteristic length. This approach is justified because the characteristic length for Reynolds number remains unchanged despite vegetation bending. The ratio of work contributions by vertical velocity can be expressed as:

$$R_W = \overline{\varepsilon_{cw,z} / \varepsilon_{cw\_w}} \tag{14}$$

where the overbar represents the average over the length of the canopy. The remaining portion of $\overline{\varepsilon_{cw\_w}}$ is attributed to the contribution of horizontal velocity.

According to Longuet-Higgins and Stewart (1961), the expression of radiation stress is:

$$S_x = E\left(\frac{1}{2} + \frac{2kh}{\sinh 2\,kh}\right) \tag{15}$$

Substituting expressions of E and S_x into Eq. (7), the wave height reduction:

$$\frac{\partial H}{\partial x} = -\frac{4}{\rho g H} \frac{\varepsilon_{cw\_w}}{(C_g + U_0) + \left(\frac{2kh}{\sinh(2kh)} + \frac{1}{2}\right) U_0} \tag{16}$$

Given the specified initial conditions, the fourth-order Runge-Kutta method with a step size of $dx = 0.1$ is applied to numerically solve Eq. (16). During this process, ε_{cw_w} is determined through a two-layer

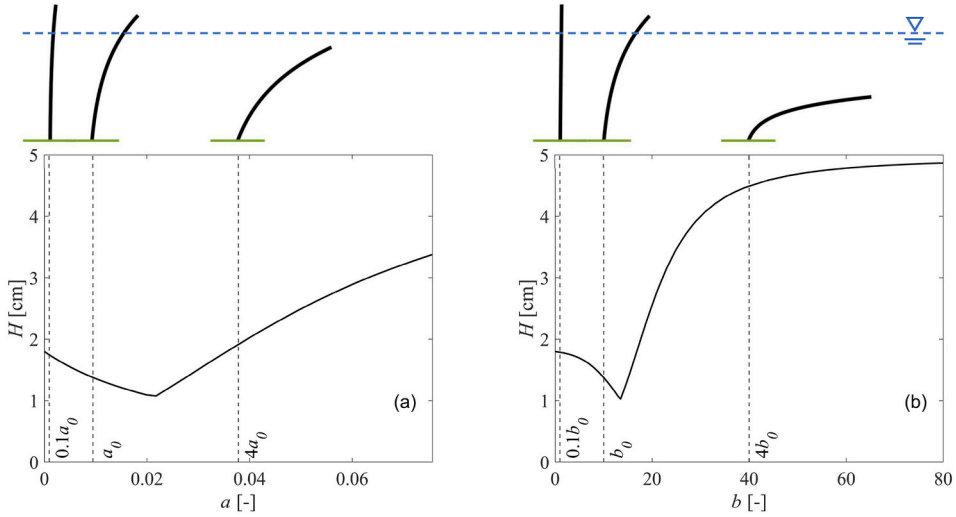

Fig. 3. Variation of residual wave height with coefficients (a) a and (b) b. The residual wave height is defined as the wave height at the end of the canopy ($x = 6$ m). The top panel depict the corresponding vegetation bending for each parameter. The blue dashed line represents the static water level. (For interpretation of the references to color in this figure legend, the reader is referred to the Web version of this article.)

numerical integration. For pure wave cases or rigid vertical vegetation, Eq. (16) can be simplified by assign zero value to U_0 and W. After obtaining the experimental results for wave height attenuation, the corresponding bending coefficient b can be determined using the Hill-Climbing method (Fig. C1).

The proposed model is designed for both pure wave and combined wave-current conditions. To validate the model's generalizability, we compared its predictions against data from both this study and independent experiments (Fig. 4). The model curve captures a fundamental physical trend: wave attenuation decreases as the bending coefficient increases. To perform a meaningful comparison that isolates the effect of bending, we selected literature data obtained under hydrodynamically similar conditions (Table A1). For these independent data points, the effective bending coefficient was inferred by applying the present model to the reported wave attenuation. The close agreement between these inferred values and the model's trend strongly supports the model's utility as a predictive tool.

The use of machine learning is essential due to the impracticality of capturing all real-world wave-current-vegetation scenarios through limited flume experiments and the unclear mechanisms linking flexible vegetation's bending coefficient to different wave, current, and vegetation conditions. The (eXtreme Gradient Boosting) XGBoost algorithm is employed to learn from datasets in this study as well as from Lei and Nepf (2019a), van Veelen et al. (2020), Zhang and Nepf (2024), and Reis et al. (2024). This machine learning model is trained to predict the bending coefficient b. By integrating analytical modeling with machine learning, a hybrid machine learning-enhanced attenuation model is developed, offering improved predictive capabilities for complex hydrodynamic interactions.

XGBoost predicts the bending coefficient b by iteratively training regression trees to minimize residuals via gradient descent.

$$b = f(Ca_{wc}, L, \alpha, \lambda, \mathrm{Re}, sf, B) \tag{17}$$

$$\begin{aligned} Ca_{wc} &= \frac{1}{2}\frac{Cd\rho b_v h_v^3}{EI}\left(U_0^2 + \frac{1}{2}U_w^2\right) \\ L &= \frac{2\pi h_v}{U_w T} \\ \alpha &= \frac{U_0}{U_w} \\ \lambda &= \frac{h_v}{h} \\ \mathrm{Re} &= \frac{(|U_{in}| + U_w)b_v}{\nu} \\ sf &= N\pi b_v^2/4 \quad \text{(cylinder)} \\ B &= \frac{\Delta\rho g \pi b_v^2 h_v^3}{4EI} \text{(cylinder)} \end{aligned} \tag{18}$$

where Ca_{wc} represents the Cauchy number in wave-current interaction, indicating vegetation flexibility relative to hydrodynamic force (Lei and Nepf, 2019b). EI is the flexural rigidity, which can be measured using three-point bending tests or tensile tests. L is the blade length ratio. α is the ratio of current velocity to the horizontal wave orbital velocity, indicating the strength of the wave-current interaction (Hu et al., 2014). λ is the submergence ratio. Re is the Reynold's number, where $\nu = 10^{-6}$ m^2/s is the kinematic viscosity. sf denotes solid volume fraction. For cylindrical vegetation mimics, the expression is provided in Eq. (18). B is the buoyancy parameter, defined by the density difference between the vegetation and water ($\Delta\rho$), was included in the initial dimensional analysis. However, it was excluded from the final model because its formulation introduces redundancy by sharing key variables with other parameters, as well as because it exhibited limited variability in our dataset, thereby offering negligible predictive information for the machine learning algorithm.

In the machine learning process, the dataset is divided into training, validation, and testing subsets (Fig. D1). The testing subset, which is not involved in the training process, serves as an independent and objective benchmark for evaluating model performance.

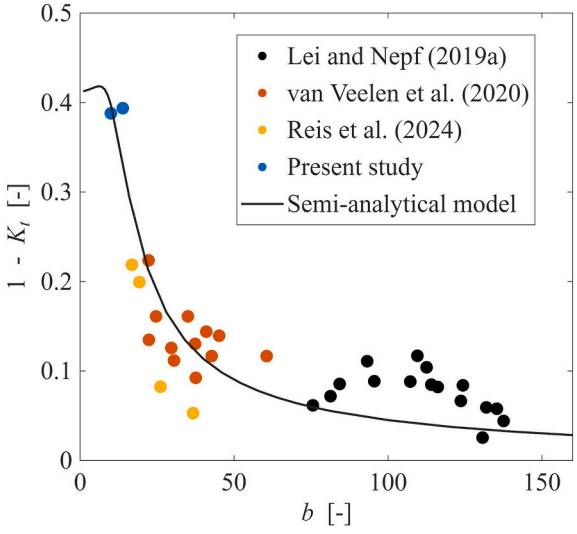

Fig. 4. Variation of wave height attenuation with bending coefficient b. 1 - K_t represents the relative wave height attenuation at the end of canopy. The curve is generated by fixing the wave parameters and varying only the bending coefficient. The bending coefficients for the literature data are determined using the calibration method proposed in this study.

3. Results

3.1. Force acting on flexible vegetation

Time-synchronized force observation data for flexible and rigid rods were transformed into phase-averaged force diagrams for comparative analysis (Fig. 5), where forces are shown in dimensional units to provide an intuitive understanding of their physical scale. It is acknowledged that a limitation of this setup is that the rigid rods were installed within a flexible canopy, thereby experiencing hydrodynamic conditions distinct from other elements in the flexible canopy. Nevertheless, this configuration was necessary to achieve synchronized force measurements. As waves propagate through the vegetated area, energy is continuously attenuated, resulting in weakened hydrodynamic forces and a reduction in the horizontal force on the vegetation (e.g. Fig. 5d–f). Fig. 5a–c introduces an additional opposing current of −6 cm/s compared to Fig. 5d–f, while Fig. 5g–i introduces an additional following current of 6 cm/s. These variations in current interactions with waves enhance the flow field's nonlinearity, thereby increasing the uncertainty of the phase-averaged force curves. The distance between the two dashed lines in each subplot indicates the phase difference in forces between the rigid and flexible rods. This phase difference is relatively small, particularly at $x = 3$ m, while the overall average across x = 1, 3, 5 m is 0.49 rad.

A linear fit of the data points reveals a slope of less than 1, indicating that under most conditions, F_{mean} on the rigid rod exceeds that on the flexible rod (Fig. 6a). The comparison of F_w on rigid and flexible rods was conducted at the same observation points (Fig. 6b). Most data points fall below the 1:1 line, particularly the crosses ($h = 33$ cm, submerged condition). This suggests that, under identical hydrodynamic

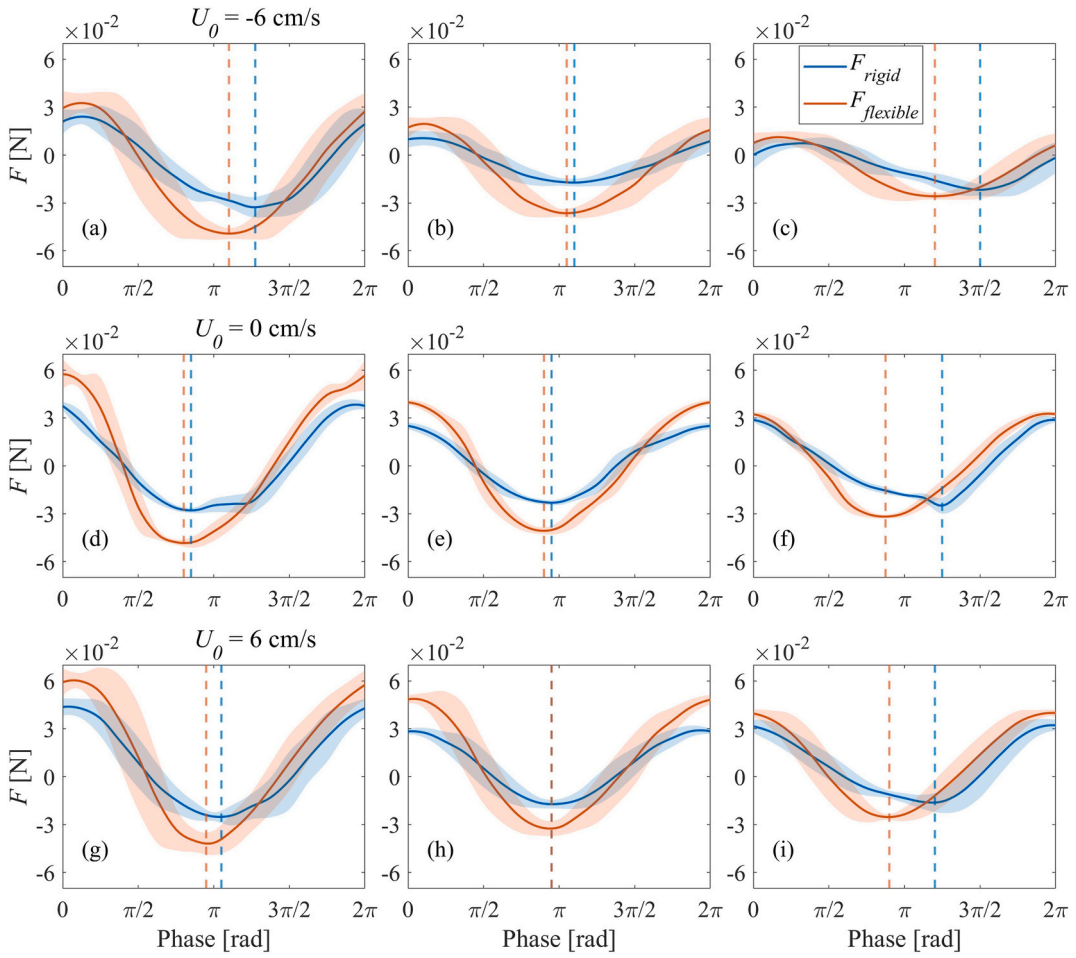

Fig. 5. Phase-averaged horizontal force on flexible and rigid mimics in case Wave0508. The results in the same row illustrate the along-path variation of forces within the canopy. For meaning of the case names, see Table 2. The left column represents measurements at $x = 1$ m, the middle column: $x = 3$ m, and the right column: $x = 5$ m. The dashed lines indicate the positions with minimum force. The shaded region represents a range of one standard deviation. U_0 is the velocity of imposed uniform current.

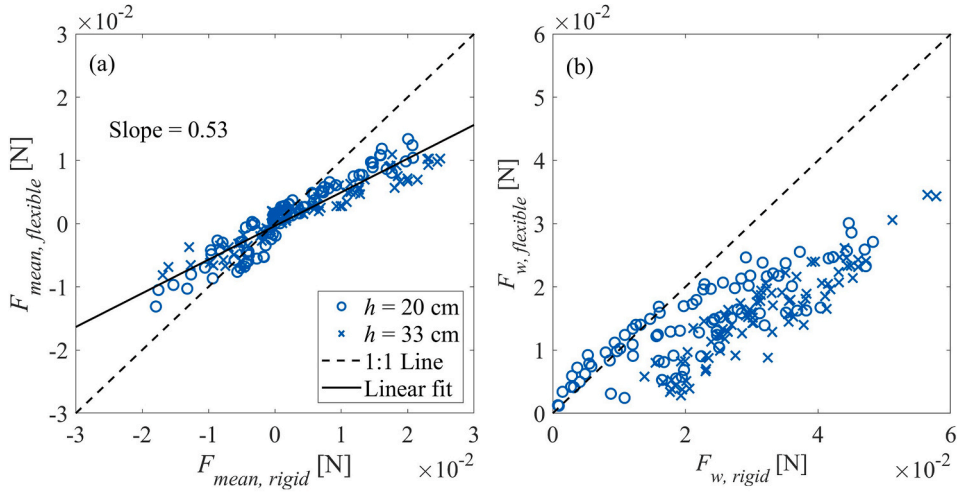

Fig. 6. Comparison of horizontal force components between flexible and rigid mimics: (a) Time-averaged mean force F_{mean}; (b) The amplitude of force fluctuation F_w. All force data presented here were recorded at $x = 3$ m.

conditions, F_w on the rigid rod is greater than that on the flexible rod.

Only a few data points, represented by circles ($h = 20$ cm), show the flexible rod experiencing a greater horizontal force, although the difference is minimal. This occurs because the entire 25 cm length of the flexible rod is submerged in water, whereas only 20 cm of the vertical rigid rod is submerged. The greater submerged length compensates for the reduction in horizontal force due to the flexible rod's swinging. From Figs. 5 and 6, it can be concluded that under identical hydrodynamic

conditions, the horizontal force exerted on the rigid rod exceeds that on the flexible rod, aligning with expected physical behavior.

3.2. Wave attenuation

Flexible vegetation exhibited a stronger wave attenuation capacity than rigid vegetation both in low and high density cases (Fig. 7). H_r denotes the relative wave height, normalized by the incident wave height H_0. The wave attenuation data for rigid vegetation were obtained from Hu et al. (2021) to compare with present study. For detailed experimental setup, refer to Fig. B2. The comparison between subplots (a-c) and (d-f) indicates that the wave height attenuation capability in near emergent cases is significantly greater than that in submerged cases. Under near-emergent conditions, the wave attenuation capacity of flexible vegetation decreases with increasing wave periods, while the opposite trend is observed under submerged conditions. This pattern is consistent with the findings of Huang et al. (2024) for rigid vegetation, indicating that a similar phenomenon may also occur in flexible vegetation.

The data points for both near-emergent and submerged conditions above the 1:1 line (Fig. 8), indicating that flexible vegetation exhibits superior wave attenuation capability compared to rigid vegetation. On average, the flexible rods can attenuate incident wave heights by 8 % more than the rigid rods in the submerged state and by 21 % in the near-emergent state. Only a few data points, corresponding to high-flow-velocity conditions, are below the 1:1 line.

Analysis of horizontal force and wave height attenuation demonstrates that flexible vegetation experiences fewer horizontal forces but can induced greater wave attenuation, suggesting the presence of additional contribution than the horizontal forces. Observations of vegetation deflection further support the hypothesis that vertical flow velocity or vertical force contributes to energy attenuation.

The proposed hybrid model exhibits significant high accuracy in predicting wave attenuation, as illustrated in Fig. 9. In the context of this study's conditions, the predictions from the Effective Length method show deviations from the experimental measurements (Fig. 9a and b). Specifically, it underestimates wave attenuation capacity in both near-emergent and submerged vegetation scenarios. The proposed hybrid model integrates experimental data from previous studies, expanding the applicability of input parameters to a wider range of wave, current, and vegetation conditions. This incorporation of external datasets enhances the model's generalization capabilities and significantly improves its predictive accuracy across diverse experimental scenarios (Fig. 9c and d). For testing subsets excluded from the machine learning training process, the hybrid model achieves a coefficient of determination (R^2) of 0.96 when comparing predicted wave attenuation results with experimental values, demonstrating its robustness and reliability.

A consistent underestimation of wave attenuation by the hybrid model was observed for the present study dataset (Fig. 9c). This systematic discrepancy suggests that exceptionally large wave attenuation may be driven by additional energy dissipation mechanisms. These include processes such as enhanced vortex shedding or interactions at the canopy-top shear layer, which are not captured in our model.

The ratio of work contributions by wave-induced vertical velocity R_w is illustrated in Fig. 10. Firstly, R_w decreases with increasing current velocity, regardless of whether the current is in the positive or negative direction. This suggests that horizontal currents, in either direction, enhance the reconfiguration of vegetation, as evidenced by an increased bending coefficient and reduced deflected height observed in this study. Secondly, a longer wave period also results in a reduction in R_w. Moreover, the impact of water depth on R_w is evident from the comparison between near-emergent and submerged conditions. The results show that greater water depth leads to a decrease in R_w, suggesting that deeper water reduces the effectiveness of vertical work in attenuating waves. Notably, R_w can reach up to 60 % under certain conditions, highlighting the significant role of vertical velocity in wave attenuation.

3.3. SHAP analysis

The SHAP (SHapley Additive exPlanations) method, grounded in cooperative game theory, was employed to interpret the XGBoost model by quantifying each feature's contribution to its output. As presented in Fig. 11, this analysis elucidates the influence of various features, with a specific focus on the bending coefficient b, thereby enhancing trust in the model's reliability. The SHAP analysis identifies Ca_{wc} and sf as the key parameters influencing vegetation deflection based on the magnitude of the slopes from the linear regression in Fig. 11b–c. Their regression slopes are substantially larger than those of all other parameters (Fig. D3). Specifically, Ca_{wc} exhibits a positive correlation with SHAP values, indicating that an increase in Ca_{wc} raises the predicted b, as higher hydrodynamic forces dominate and promote greater vegetation deflection. In contrast, sf shows a negative correlation, suggesting

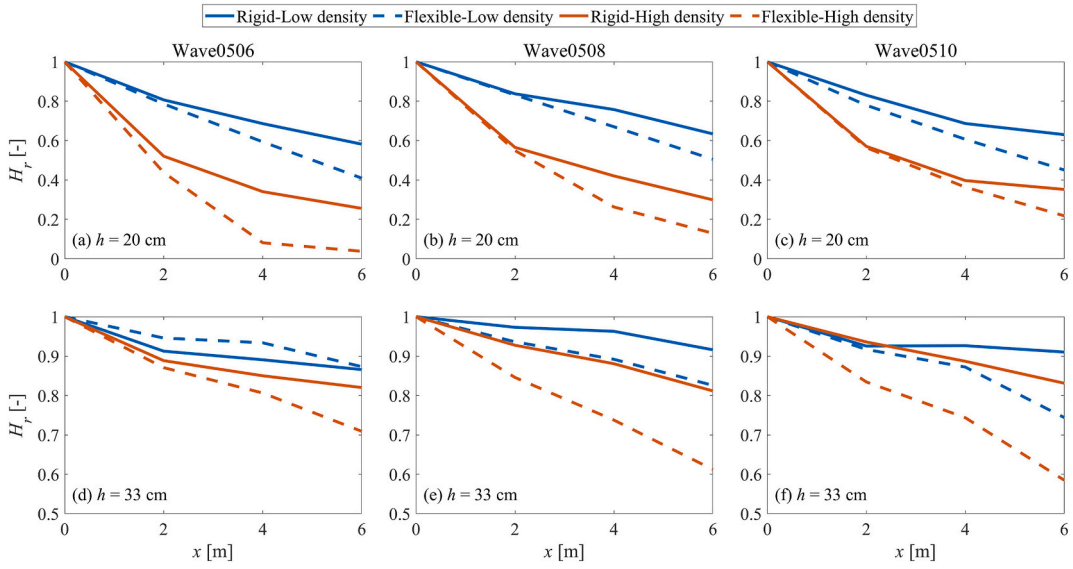

Fig. 7. Comparison of wave propagation through rigid and flexible vegetation: (a, d) Wave0506, (b, e) Wave0508, and (c, h) Wave0510 in pure wave conditions. The first row represents near-emergent conditions with water depth $h = 20$ cm, while the second row represents submerged conditions with water depth $h = 33$ cm. For detailed case descriptions, refer to Table 2. The solid lines represent rigid vegetation, while the dashed lines represent flexible vegetation.

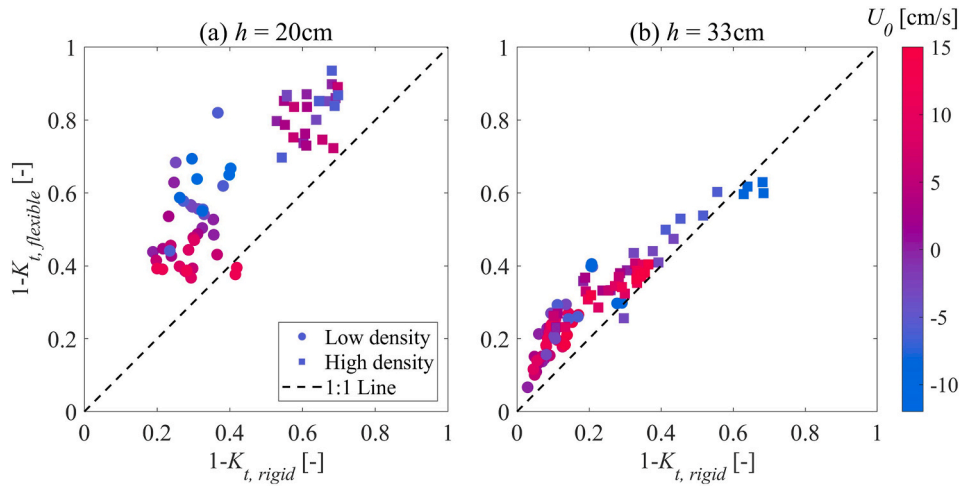

Fig. 8. Comparison of relative wave attenuation between flexible and rigid canopy: (a) Near-emergent condition with water depth h = 20 cm. (b) Submerged conditions with water depth h = 33 cm. 1 - K_t is the relative wave height attenuation at the end of canopy. Marker color represents the velocity of imposed uniform current U_0. (For interpretation of the references to color in this figure legend, the reader is referred to the Web version of this article.)

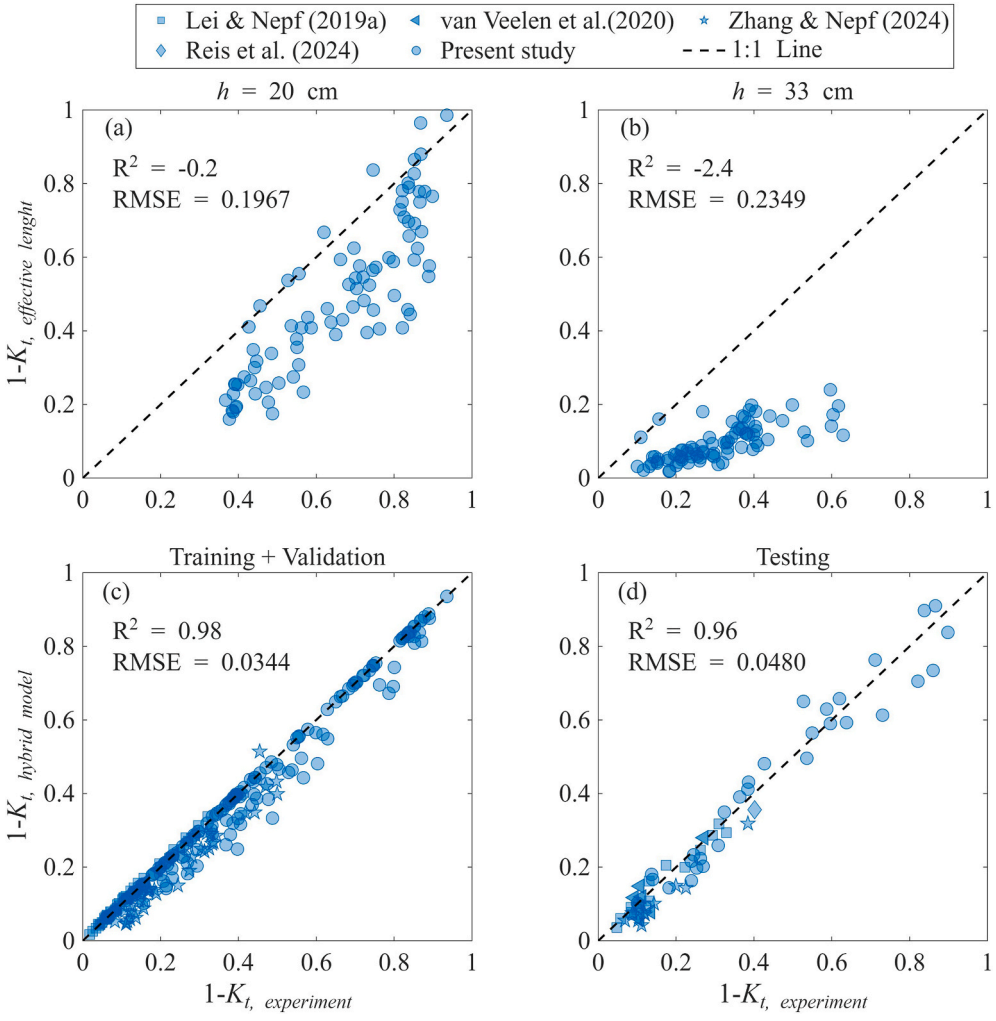

Fig. 9. Comparison of wave height attenuation using (a, b) the Effective Length method and (c, d) the presented hybrid model. The empirical formula for the effective length in combined wave-current flow is proposed by Lei and Nepf (2019b) as $l_e/h_v = 0.9Ca_{wc}^{-1/3}$.

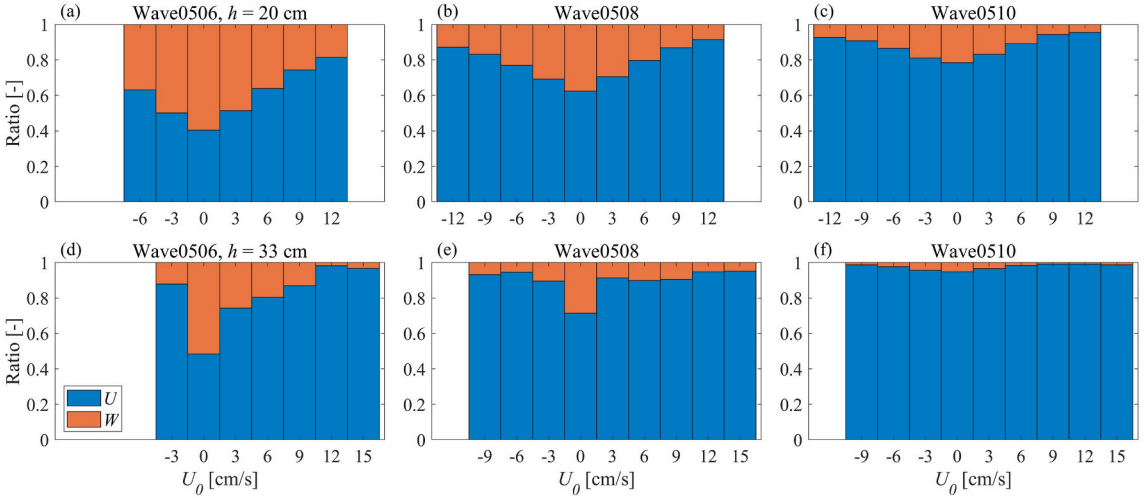

Fig. 10. Ratio of work contributions by vertical (W) and horizontal (U) in wave attenuation process across different U_0. The first row represents near-emergent conditions with water depth $h = 20$ cm, while the second row represents submerged conditions with water depth $h = 33$ cm. The ratio of work contributions by wave induced vertical velocity, R_w, is determined by spatial-averaged dissipation term, as defined in Eq. (14). For meaning of the case names, see Table 2. Red columns represent R_w. U_0 is the velocity of imposed uniform current. (For interpretation of the references to color in this figure legend, the reader is referred to the Web version of this article.)

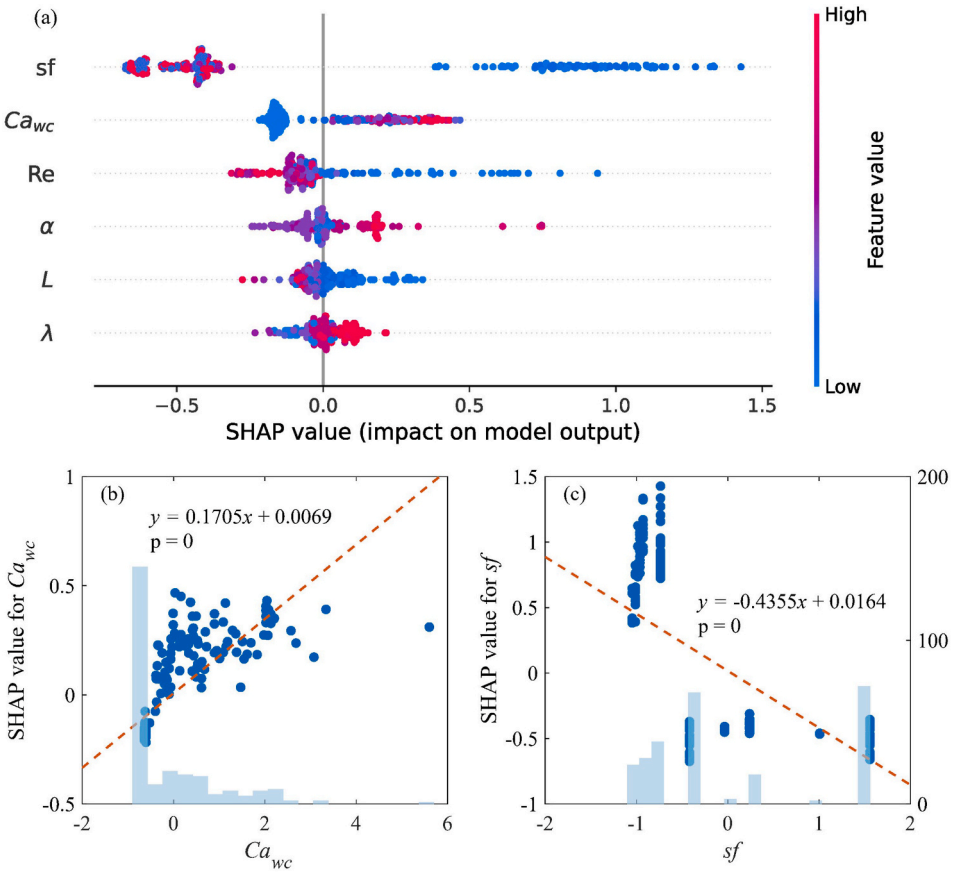

Fig. 11. (a) SHAP Variance importance plot. The x-axis represents the SHAP values, which quantify each feature's contribution to predicting b. The input features are ranked on the left in descending order of their impact. The pile up of points indicates a high concentration of data points with similar SHAP values. Marker color represents the values of feature. (b–c) Linear regression analysis of standardized features and SHAP values. The x-axis represents the standardized feature values and the y-axis represents the corresponding SAHP values. The secondary y-axis on the right represents the number of occurrences of data points within each bin. (For interpretation of the references to color in this figure legend, the reader is referred to the Web version of this article.)

that an increase in sf reduces the predicted b, since denser vegetation distributes hydrodynamic forces across more elements, thereby reducing deflection.

The feature rankings in Fig. 11a are consistent with the regression slopes observed in the linear regression analysis of standardized features. Furthermore, the scatter plots for Ca_{wc}, L, α, Re, and sf exhibit a

consistent trend: as the input feature values increase to a certain threshold, their influence on the model output stabilizes, indicating that their effect on b plateaus. This analysis provides valuable insights into the model's internal mechanisms and enhances the understanding of how hydrodynamic and structural parameters influence vegetation deflection.

4. Discussion

4.1. The role of vertical forces in wave attenuation

Flexible vegetation typically bends and oscillates under hydrodynamic forces, reducing mechanical stress and preventing structural damage—a classic trade-off mechanism in ecological systems (Bouma et al., 2005). It is widely accepted that the oscillatory motion of flexible vegetation modifies the velocity term in the Morison equation to a relative velocity, thereby reducing horizontal forces on the vegetation and, consequently, its wave attenuation capacity (Bradley and Houser, 2009; Zeller et al., 2014; Leclercq and de Langre, 2018). However, contrary to this conventional understanding, our experiments demonstrate that flexible vegetation may exhibit stronger wave attenuation compared to rigid vegetation. This finding challenges the traditional perspective and calls for a reevaluation of the mechanisms underlying wave attenuation by flexible vegetation.

Our findings challenge the prevailing literature by demonstrating that flexible vegetation can outperform rigid vegetation in wave attenuation. However, this superior performance is confined to small-excursion stems conditions. A similar observation was made by Liu et al. (2023), who attributed this phenomenon to the phase difference between vegetation motion and water motion, as proposed by Mullarney and Henderson (2010). Specifically, when vegetation motion is 90° out of phase with water motion, the resultant relative velocity between the vegetation and water increases. This enhanced relative velocity leads to greater forces on flexible vegetation compared to rigid vegetation, as documented by Luhar and Nepf (2016). However, our experimental results challenge this explanation. Contrary to the aforementioned studies, our data reveal that rigid rods experienced greater horizontal forces than flexible rods, and no significant phase difference was observed (see Fig. 5). This inconsistency suggests that the phase difference mechanism alone is insufficient to explain the observed wave attenuation, thereby highlighting the need to investigate alternative mechanisms.

In our experiments, the ratio of vegetation rigidity to hydrodynamic forces Ca_{wc} was predominantly less than 10. The flexible vegetation did not exhibit significant horizontal oscillation; instead, it displayed a bobbing motion with unidirectional tilting under flow influence (see Fig. 3b in Jacobsen et al., 2019 and Fig. 6 in Lei and Nepf, 2019a). Under near-emergent conditions, the enhanced attenuation is mainly attributed to the increased effective submerged biomass of flexible vegetation compared to its upright rigid counterpart. While under submerged conditions, the reduced deflected height of vegetation decreases the work done by horizontal velocities, this reduction is compensated by an increased energy dissipation contribution from the wave-induced vertical velocity. This mechanism explains why flexible vegetation can induce stronger wave attenuation under limited reconfiguration. For simplicity, our analytical model omits the effects of plant motion, approximating flexible vegetation as bent and rigid vegetation. Despite this simplification, the model successfully replicates the observed attenuation discrepancy, underscoring the critical role of vertical forces in the process.

4.2. A hybrid model for wave attenuation by flexible vegetation

The novel hybrid modeling framework proposed in this study effectively integrates a machine learning predictor with a semi-analytical model to simulate the influence of flexible vegetation on wave attenuation. By incorporating a bending coefficient b, the model accurately represents the vegetation's bending characteristics and quantifies its contribution to wave attenuation. Additionally, the semi-analytical model accounts for the effect of wave-induced vertical flow velocity on wave attenuation, thereby enhancing the model's comprehensiveness.

The predictor was trained and validated using experimental and literature data, exhibiting high predictive accuracy. Notably, the semi-analytical model successfully reproduced the effects of wave-induced vertical flow velocity on wave height attenuation. However, the model's performance remains partially dependent on the quality and diversity of the training data, indicating that additional experimental data may be necessary to enhance its robustness and generalization capability, particularly under extreme environmental conditions.

Compared to the Modified Drag Coefficient method, the hybrid model provides a significant advantage by distinguishing individual contributions to wave attenuation, thereby facilitating a more precise analysis of the key driving processes. In contrast to the Effective Length method, which ignores wave-induced vertical flow velocities, the hybrid model explicitly incorporates these contributions, resulting in a more comprehensive representation of wave energy attenuation. Additionally, the hybrid model outperforms the HSB method by accommodating wave-current interaction, substantially expanding its applicability across diverse environmental scenarios.

4.3. Limitation and future potential of the hybrid model

The equivalent rigid vegetation model may oversimplify the complex dynamic interactions between flexible vegetation and wave-current systems. Moreover, the assumption of two-dimensional flow disregards the three-dimensional swaying motions of flexible vegetation, which play a crucial role in turbulent kinetic energy production (Fu et al., 2023). Vortex shedding induced by oscillating vegetation is a potential mechanism for energy dissipation (Houseago et al., 2022; Luhar and Nepf, 2016). Recent work by Vettori et al. (2025) has advanced the understanding by modeling wave attenuation induced by the shear layer at the canopy top. Further investigation into these and related processes will lead to a more comprehensive understanding of wave attenuation mechanisms.

Enhancing the model by incorporating a more detailed representation of turbulence dissipation mechanisms could potentially improve its ability to simulate wave energy transfer and attenuation processes with greater accuracy. Additionally, integrating experimental data from extreme wave-current conditions and field data from storm surges into machine learning frameworks could refine the model's predictive performance and enhance its applicability to extreme scenarios. Such advancements would establish the model as a more robust tool for evaluating wave attenuation by vegetation and support the development of more effective and sustainable coastal engineering solutions, particularly in the context of escalating climate-driven challenges.

5. Conclusion

This study developed an efficient assessment method for wave attenuation by flexible vegetation under wave-current interactions, providing a practical tool for coastal engineering and ecosystem management. The experimental results demonstrate that flexible vegetation exhibits superior wave attenuation performance compared to rigid vegetation in small-excursion stems conditions. Besides, the horizontal force exerted on the rigid rod was observed to be greater than that on the flexible rod. Our model conceptualizes flexible vegetation as rigid but bent cylinders, and incorporates the contribution of wave-induced vertical velocity to the wave attenuation. The hydrodynamic-induced deflection of flexible vegetation was effectively characterized by a bending coefficient b, which was accurately predicted using a data-driven approach. The robustness of the method was validated by the

experimental data from this study and supplementary datasets from the literature.

The data analysis reveals that vertical velocity accounts for up to 60 % of the work in wave attenuation. This finding highlights the importance of considering vertical flow velocity when assessing wave energy attenuation by flexible vegetation. Moreover, SHAP analysis identifies the solid volume fraction and the Cauchy number as the primary factors influencing vegetation deflection. An increase in the solid volume fraction reduces the drag on individual vegetation elements, making them less susceptible to bending. In contrast, a higher Cauchy number promotes vegetation deflection, resulting in an increased bending coefficient. This study provides new insights into quantifying vegetation-induced wave energy attenuation.

CRediT authorship contribution statement

Weifeng Ye: Writing – review & editing, Writing – original draft, Visualization, Validation, Methodology, Formal analysis, Data curation. **Zhan Hu:** Writing – review & editing, Writing – original draft, Supervision, Funding acquisition. **Khanh Linh Phan:** Writing – review & editing. **Marcel Stive:** Writing – review & editing.

Declaration of generative AI and AI-assisted technologies in the writing process

During the preparation of this work the authors used ChatGPT (https://openai.com/chatgpt) in order to improve readability and language. After using this tool, the authors reviewed and edited the content as needed and take full responsibility for the content of the publication.

Declaration of competing interest

The authors declare that they have no known competing financial interests or personal relationships that could have appeared to influence the work reported in this paper.

Acknowledgments

The authors would like to thank the members of M5 (Mudflat, Marsh, Mangrove, Measurement & Modeling) Lab at Sun Yat-sen University for their assistance in the flume experimental works. This work was supported by National Natural Science Foundation of China (No. 42176202), Innovation Group Project of Southern Marine Science and Engineering Guangdong Laboratory (Zhuhai; Grant No. 311021004), Guangdong Provincial Department of Science and Technology (2019ZT08G090).

Appendix A. Vertical profiles of time-mean velocity

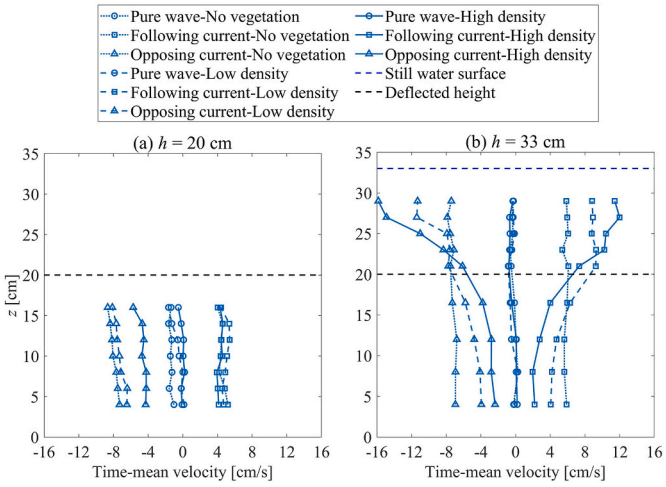

Fig. A1. Vertical profiles of time-mean velocity in (a) near-emergent and (b) submerged canopies under different density conditions. $H = 5$ cm, $T = 0.8$ s and $U_0 = \pm 6$ cm/s.

Vertical profiles of time-mean velocity were measured under both near-emergent and submerged conditions at the center of the canopy ($x = 3$ m). The deflected height of the vegetation mimics was set at 20 cm (Fig. A1). These measurements encompassed 60 % and 76 % of the total water depth for near-emergent and submerged conditions, respectively. Below the deflected height, the horizontal velocity distribution remained relatively uniform. An increase in vegetation density resulted in a reduction of flow velocity within the canopy region.

Table A1
Selection of data for wave attenuation comparison.

	H [cm]	h [cm]	h_v [cm]	T [s]	N_v [stems/m^2]	b_v [mm]
Lei and Nepf (2019a)	2.8–10.2	45	15	1.4, 2	600	3
van Veelen et al. (2020)	10–20	40, 50	30	1.4, 2	1111	5
Reis et al. (2024)	14, 15	35	25	1.4, 2	220, 440	10
Present study	5, 7	33	25	1.0	556	10

Appendix B. Additional experimental setup

In present experiment, each measurement location was equipped with two force sensors. Some vegetation mimics were removed to create an 8 cm

gap to avoid collisions with the flexible vegetation and the sensors during experiments (Fig. B1). While the removal of mimics around the sensors creates localized discontinuities in the vegetated area, potentially leading to three-dimensional effects in shear stress and turbulent kinetic energy distribution at the canopy-water interface, these local phenomena are not the focus of the present model.

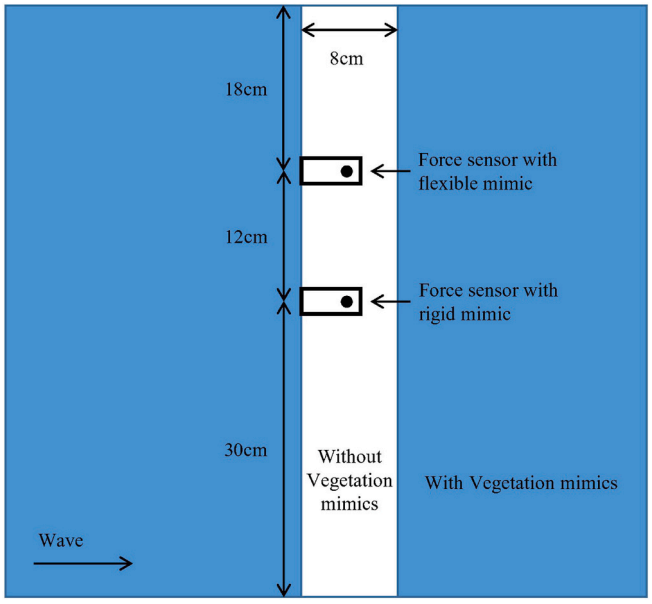

Fig. B1. Schematic of the sensor configuration and local vegetation removal.

The experiments conducted in the present study utilized the same flume as described by Hu et al. (2021). The vegetation zone length, vegetation density, water depth, and current velocity were maintained consistently across both experiments (Fig. B2). The vegetation mimics employed in both studies were identical in size, each measuring 25 cm in length and 1 cm in diameter. The comparison of wave height attenuation was performed under identical working conditions. This setup facilitates a direct and meaningful comparison of wave attenuation performance between rigid and flexible rods, offering valuable insights into the effects of different factors on wave height attenuation in the presence of vegetation mimics.

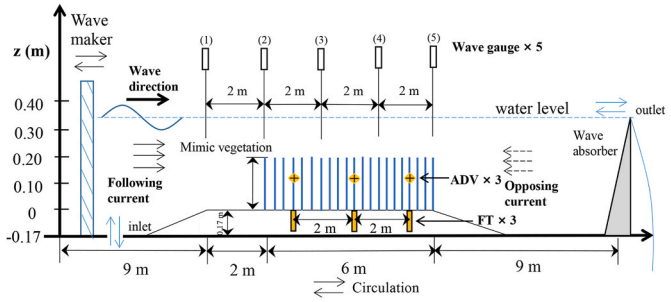

Fig. B2. Diagram of the flume experiments with rigid vegetation (Hu et al., 2021). FT is the force transducer that can measure the total force on a mimic stem. ADV is the Acoustic Doppler Velocimeter that can measure the velocity.

Appendix C. Calibration of bending coefficient

The detailed calibration procedure consists of the following steps:

1. Assign an initial value and step size for b. Calculate the wave height errors at three points, b (i-1), b(i), and b (i+1), in comparison to the experimental values. The Hill-Climbing method initiates the search in the direction of decreasing errors until a turning point is identified between b (i-1) and b (i+1).
2. Reduce the step size, and the Hill-Climbing method continues the search until the turning point is captured again.
3. Repeat step 2 until the precision requirement is satisfied.

During calibration, it is possible for the experimental residual wave height to correspond to two bending coefficients. In such cases, the initial value of the bending coefficient is set to a value greater than the turning point, enabling the Hill-Climbing method to automatically identify the nearest solution. This approach ensures an accurate and efficient calibration process.

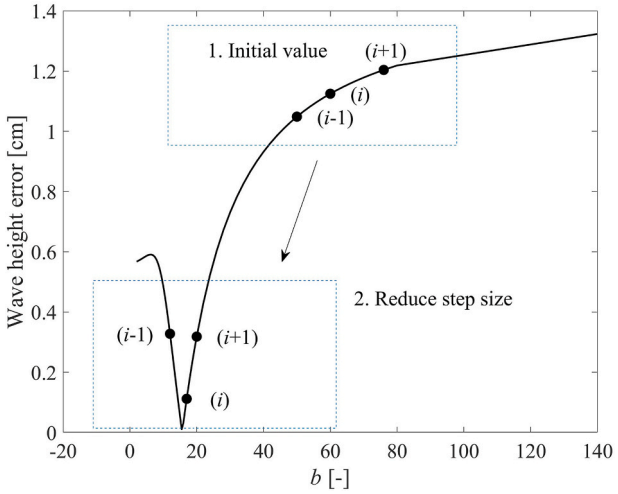

Fig. C1. Calibration of bending coefficient b using Hill-Climbing method. The y-axis represents the absolute difference between the experimental values of wave height at the end of canopy and the results from the semi-analytical model.

Appendix D. Data partitioning, SHAP model interpretation, and comparison of bending coefficients

The dataset consists of 317 samples from various experiments, including those conducted in this study as well as by Lei and Nepf (2019a), van Veelen et al. (2020), Zhang and Nepf (2024), and Reis et al. (2024). The data was strategically divided to enhance the machine learning process (Fig. D1). Using the Maximum Dissimilarity Algorithm (MDA), 60 % of the data was selected as the training set to represent the data space. The remaining data was equally divided into validation and testing sets through random allocation (Camus et al., 2011; Shi et al., 2019; Wang et al., 2021). The six input parameters were standardized before being fed into the XGBoost model to predict bending coefficient b. As a gradient-boosting framework, XGBoost operates by iteratively training sequential weak regression trees to minimize loss functions through gradient descent optimization, with each successive tree targeting the residual errors (mathematically represented as negative gradients) from preceding models.

Fig. D2 illustrates the predictive performance of the trained model. The results show that both the training and validation sets, which were part of the machine learning process, align closely with the 1:1 line, indicating excellent predictive accuracy. Additionally, the testing set, which was not involved in the training process, demonstrated satisfactory predictive performance, highlighting the model's robustness and generalizability to unseen data.

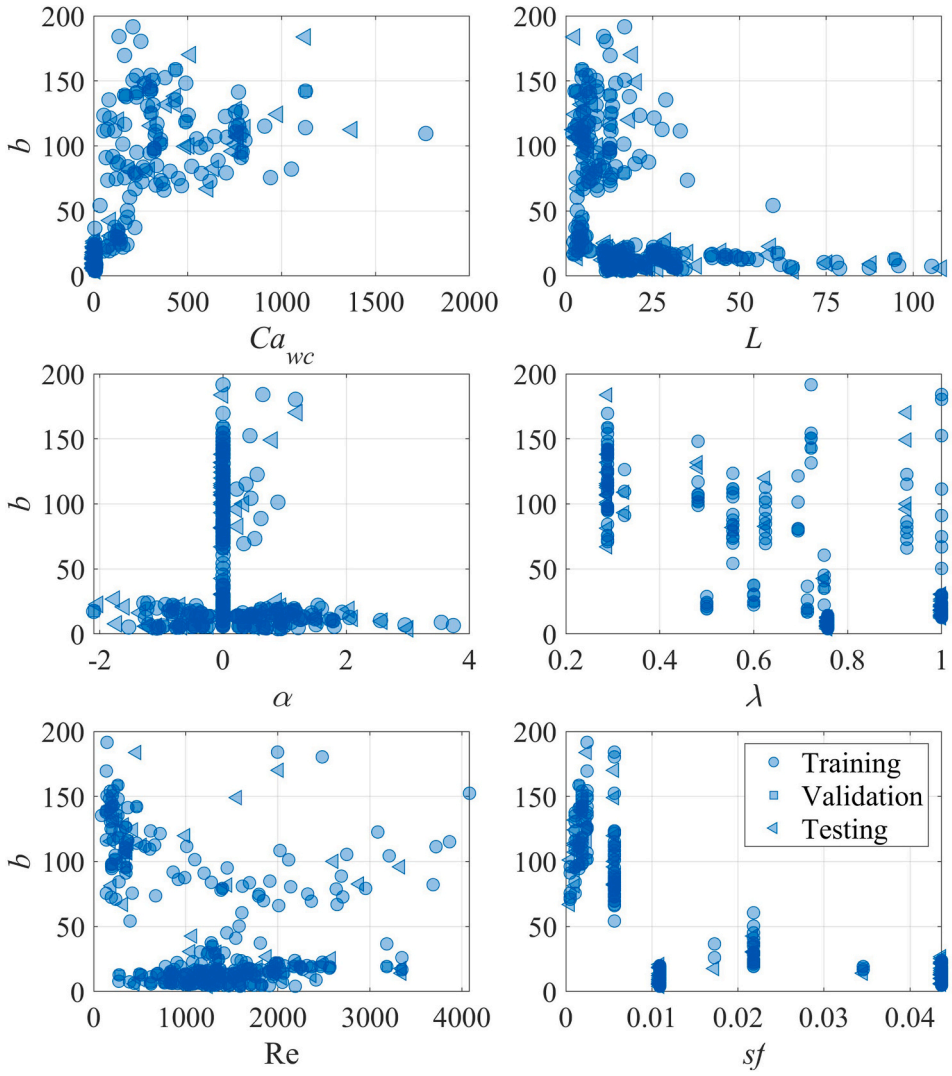

Fig. D1. Data partitioning through integration of MDA algorithm and random allocation. The data set is split into training, validation, and testing subsets, with the testing set used independently to objectively evaluate model performance.

Machine learning algorithms are often considered black boxes, as they lack transparency in explaining the internal mechanisms behind their predictions. SHAP provides a solution by quantitatively analyzing the influence of each input parameter on the output (Lundberg and Lee, 2017):

A SHAP value greater than 0 indicates a positive effect on the target variable, meaning the feature contributes positively to the predicted value. Conversely, a SHAP value less than 0 implies a negative effect, where the feature reduces the predicted value. SHAP values can be visualized to provide clear insights into the contributions of each feature, allowing for more interpretable and transparent model behavior.

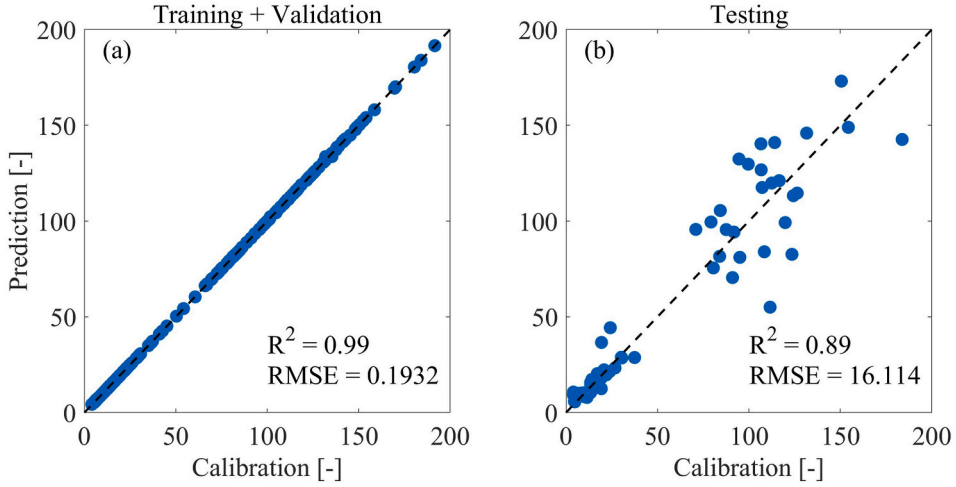

Fig. D2. Comparison of predicted and calibrated values of the bending coefficients *b*.

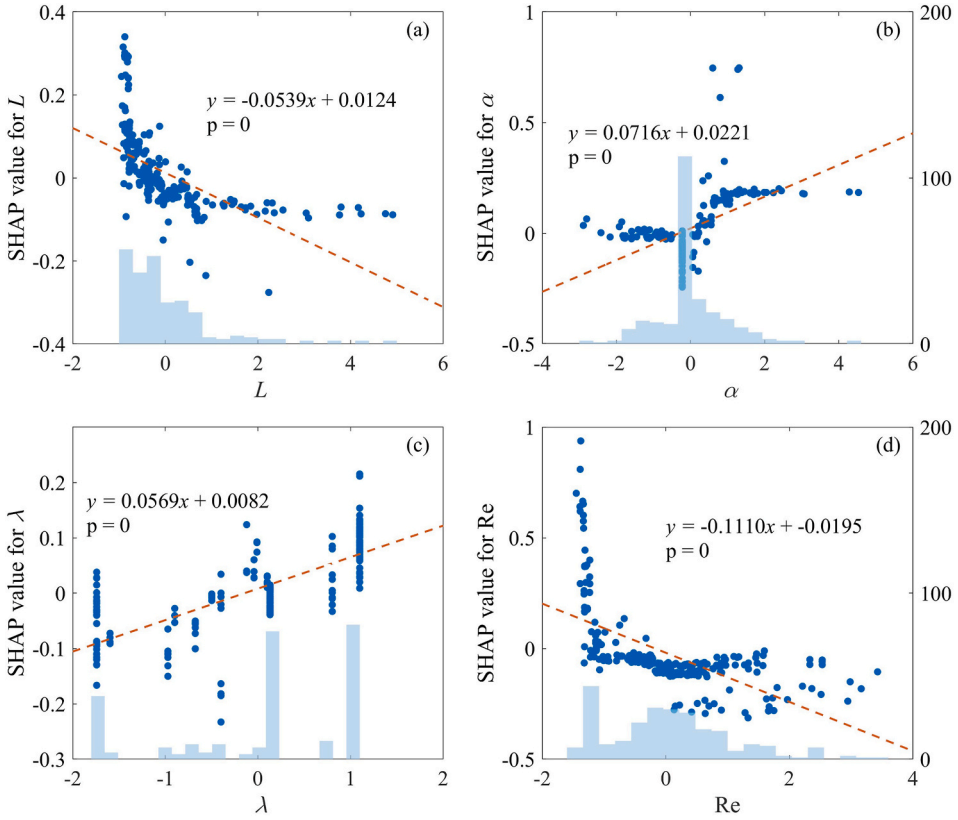

Fig. D3. Linear regression analysis of standardized features and SHAP values.

Appendix E. Supplementary data

Supplementary data to this article can be found online at https://doi.org/10.1016/j.oceaneng.2025.123975.

References

Anderson, M.E., Smith, J.M., 2014. Wave attenuation by flexible, idealized salt marsh vegetation. Coast. Eng. 83, 82–92. https://doi.org/10.1016/j.coastaleng.2013.10.004.

Augustin, L.N., Irish, J.L., Lynett, P., 2009. Laboratory and numerical studies of wave damping by emergent and near-emergent wetland vegetation. Coast. Eng. 56, 332–340. https://doi.org/10.1016/j.coastaleng.2008.09.004.

Barbier, E.B., Hacker, S.D., Kennedy, C., Koch, E.W., Stier, A.C., Silliman, B.R., 2011. The value of estuarine and coastal ecosystem services. Ecol. Monogr. 81 (1), 169–193. https://doi.org/10.1890/10-1510.

Bouma, T.J., De Vries, M.B., Low, E., Peralta, G., Tánczos, I.C., van de Koppel, J., Herman, P.M.J., 2005. Trade-offs related to ecosystem engineering: a case study on stiffness of emerging macrophytes. Ecology 86, 2187–2199. https://doi.org/10.1890/04-1588.

Bradley, K., Houser, C., 2009. Relative velocity of seagrass blades: implications for wave attenuation in low-energy environments. J. Geophys. Res. 114, F01004. https://doi.org/10.1029/2007JF000951.

Chen, H., Zou, Q., 2019. Effects of following and opposing vertical current shear on nonlinear wave interactions. Appl. Ocean Res. 89, 23–35. https://doi.org/10.1016/j.apor.2019.04.001.

Camus, P., Mendez, F.J., Medina, R., Cofiño, A.S., 2011. Analysis of clustering and selection algorithms for the study of multivariate wave climate. Coast. Eng. 58, 453–462. https://doi.org/10.1016/j.coastaleng.2011.02.003.

Chen, Z., Jiang, C., Nepf, H., 2013. Flow adjustment at the leading edge of a submerged aquatic canopy. Water Resour. Res. 49, 5537–5551. https://doi.org/10.1002/wrcr.20403.

Dalrymple, R.A., Kirby, J.T., Hwang, P.A., 1984. Wave diffraction due to areas of energy dissipation. J. Waterw. Port, Coast. Ocean Eng. 110 (67), 67–79. https://doi.org/10.1061/(ASCE)0733-950X(1984)110:1.

Daro Justine, Y.E., Seenath, A., 2025. Vegetative nature-based solutions for coastal flood risk management: benefits, challenges, and uncertainties. Ocean Coast Manag. 261, 107520. https://doi.org/10.1016/j.ocecoaman.2024.107520.

El Rahi, J., Martínez-Estévez, I., Tagliafierro, B., Domínguez, J.M., Crespo, A.J.C., Stratigaki, V., Suzuki, T., Troch, P., 2023. Numerical investigation of wave-induced flexible vegetation dynamics in 3D using a coupling between DualSPHysics and the FEA module of project chrono. Ocean. Eng. 285, 115227. https://doi.org/10.1016/j.oceaneng.2023.115227.

Fu, J., He, G., Huang, L., Dey, S., Fang, H., 2023. Swaying motions of submerged flexible vegetation. J. Fluid Mech. 971, A14. https://doi.org/10.1017/jfm.2023.587.

Houseago, R.C., Hong, L., Cheng, S., Best, J.L., Parsons, D.R., Chamorro, L.P., 2022. On the turbulence dynamics induced by a surrogate seagrass canopy. J. Fluid Mech. 934, A17. https://doi.org/10.1017/jfm.2021.1142.

Hu, Z., Lian, S., Wei, H., Li, Y., Stive, M., Suzuki, T., 2021. Laboratory data on wave propagation through vegetation with following and opposing currents. Earth Syst. Sci. Data 13, 4987–4999. https://doi.org/10.5194/essd-13-4987-2021.

Hu, Z., Suzuki, T., Zitman, T., Uittewaal, W., Stive, M., 2014. Laboratory study on wave dissipation by vegetation in combined current–wave flow. Coast. Eng. 88, 131–142. https://doi.org/10.1016/j.coastaleng.2014.02.009.

Huang, K., Hu, Z., Liu, Z., Paul, M., Xu, T., Suzuki, T., 2024. Pinpointing the role of wave period in vegetation induced wave attenuation. Coast. Eng., 104568 https://doi.org/10.1016/j.coastaleng.2024.104568.

Jacobsen, N.G., Bakker, W., Uijttewaal, W.S.J., Uittenbogaard, R., 2019. Experimental investigation of the wave-induced motion of and force distribution along a flexible stem. J. Fluid Mech. 880, 1036–1069. https://doi.org/10.1017/jfm.2019.739.

Leclercq, T., de Langre, E., 2018. Reconfiguration of elastic blades in oscillatory flow. J. Fluid Mech. 838, 606–630. https://doi.org/10.1017/jfm.2017.910.

Lee, E.I.H., Nepf, H., 2024. Marsh restoration in front of seawalls is an economically justified nature-based solution for coastal protection. Commun. Earth Environ. 5, 605. https://doi.org/10.1038/s43247-024-01753-5.

Lei, J., Nepf, H., 2019a. Wave damping by flexible vegetation: connecting individual blade dynamics to the meadow scale. Coast. Eng. 147, 138–148. https://doi.org/10.1016/j.coastaleng.2019.01.008.

Lei, J., Nepf, H., 2019b. Blade dynamics in combined waves and current. J. Fluid Struct. 87, 137–149. https://doi.org/10.1016/j.jfluidstructs.2019.03.020.

Li, J., Wang, W., Dong, F., Peng, W., Fan, J., Zhao, H., Chou, Q., Huang, A., 2024. New drag force formula of bending stems in deriving analytical solutions of velocity profile for flow through flexible vegetation. Water Resour. Res. 60. https://doi.org/10.1029/2023WR035951 e2023WR035951.

Liu, S., Xu, S., Yin, K., 2023. Optimization of the drag coefficient in wave attenuation by submerged rigid and flexible vegetation based on experimental and numerical studies. Ocean. Eng. 285, 115382. https://doi.org/10.1016/j.oceaneng.2023.115382.

Longuet-Higgins, M.S., Stewart, R.W., 1961. The changes in amplitude of short gravity waves on steady non-uniform currents. J. Fluid Mech. 10, 529. https://doi.org/10.1017/S0022112061000342.

Lopez-Arias, F., Maza, M., Lara, J.L., Losada, I.J., 2023. A new predictive tool for modeling wave attenuation produced by saltmarshes in SWAN based on standing biomass. Coast. Eng. 185, 104380. https://doi.org/10.1016/j.coastaleng.2023.104380.

Losada, I.J., Maza, M., Lara, J.L., 2016. A new formulation for vegetation-induced damping under combined waves and currents. Coast. Eng. 107, 1–13. https://doi.org/10.1016/j.coastaleng.2015.09.011.

Luhar, M., Nepf, H.M., 2016. Wave-induced dynamics of flexible blades. J. Fluid Struct. 61, 20–41. https://doi.org/10.1016/j.jfluidstructs.2015.11.007.

Lundberg, S.M., Lee, S.-I., 2017. A unified approach to interpreting model predictions. In: Proceedings of the 31st International Conference on Neural Information Processing Systems, NIPS'17. Curran Associates Inc., Red Hook, NY, USA, pp. 4768–4777.

Ma, Y., Zhu, L., Peng, Z., Xue, L., Zhao, W., Li, T., Lin, S., Bouma, T.J., Hofland, B., Dong, C., Li, X., 2023. Wave attenuation by flattened vegetation (Scirpus mariqueter). Front. Mar. Sci. 10, 1106070. https://doi.org/10.3389/fmars.2023.1106070.

Maza, M., Lara, J.L., Losada, I.J., 2022. A paradigm shift in the quantification of wave energy attenuation due to saltmarshes based on their standing biomass. Sci. Rep. 12, 13883. https://doi.org/10.1038/s41598-022-18143-6.

Mendez, F.J., Losada, I.J., 2004. An empirical model to estimate the propagation of random breaking and nonbreaking waves over vegetation fields. Coast. Eng. 51, 103–118. https://doi.org/10.1016/j.coastaleng.2003.11.003.

Morris, R.L., Konlechner, T.M., Ghisalberti, M., Swearer, S.E., 2018. From grey to green: efficacy of eco-engineering solutions for nature-based coastal defence. Glob. Change Biol. 24, 1827–1842. https://doi.org/10.1111/gcb.14063.

Mullarney, J.C., Henderson, S.M., 2010. Wave-forced motion of submerged single-stem vegetation. J. Geophys. Res. 115, C12061. https://doi.org/10.1029/2010JC006448.

Reis, R.A., Fortes, C.J.E.M., Rodrigues, J.A., Hu, Z., Suzuki, T., 2024. Experimental study on drag coefficient of flexible vegetation under non-breaking waves. Ocean. Eng. 296, 117002. https://doi.org/10.1016/j.oceaneng.2024.117002.

Schaefer, R., Nepf, H., 2022. Wave damping by seagrass meadows in combined wave-current conditions. Limnol. Oceanogr. Lett. 12102. https://doi.org/10.1002/lno.12102.

Shi, H., Liang, X., Huai, W., Wang, Y., 2019. Predicting the bulk average velocity of open-channel flow with submerged rigid vegetation. J. Hydrol. 572, 213–225. https://doi.org/10.1016/j.jhydrol.2019.02.045.

Temmerman, S., Horstman, E.M., Krauss, K.W., Mullarney, J.C., Pelckmans, I., Schoutens, K., 2023. Marshes and mangroves as nature-based coastal storm buffers. Ann. Rev. Mar. Sci 15. https://doi.org/10.1146/annurev-marine-040422-092951 annurev-marine-040422-092951.

van Veelen, T.J., Karunarathna, H., Reeve, D.E., 2020. Modelling wave attenuation by quasi-flexible coastal vegetation. Coast. Eng., 103820 https://doi.org/10.1016/j.coastaleng.2020.103820.

Van Veelen, T.J., Nepf, H., Hulscher, S.J.M.H., Borsje, B.W., 2025. The thresholds of sediment resuspension within emergent vegetation under combined wave-current conditions – a flume experiment. Coast. Eng., 104727 https://doi.org/10.1016/j.coastaleng.2025.104727.

Vettori, D., Giordana, F., Manes, C., 2025. Turbulence enhances wave attenuation of seagrass in combined wave–current flows. Proc. Natl. Acad. Sci. USA 122, e2414150122. https://doi.org/10.1073/pnas.2414150122.

Vettori, D., Pezzutto, P., Bouma, T.J., Shahmohammadi, A., Manes, C., 2024. On the wave attenuation properties of seagrass meadows. Coast. Eng. 189, 104472. https://doi.org/10.1016/j.coastaleng.2024.104472.

Wang, J., He, G., Dey, S., Fang, H., 2022. Fluid–structure interaction in a flexible vegetation canopy in an open channel. J. Fluid Mech. 951, A41. https://doi.org/10.1017/jfm.2022.899.

Wang, Y., Yin, Z., Liu, Y., 2021. Predicting the bulk drag coefficient of flexible vegetation in wave flows based on a genetic programming algorithm. Ocean. Eng. 223, 108694. https://doi.org/10.1016/j.oceaneng.2021.108694.

Ye, W., Hu, Z., 2023. A new model for quantifying wave damping by vegetation in combined wave–current flow. Ocean. Eng. 288, 116119. https://doi.org/10.1016/j.oceaneng.2023.116119.

Zeller, R.B., Weitzman, J.S., Abbett, M.E., Zarama, F.J., Fringer, O.B., Koseff, J.R., 2014. Improved parameterization of seagrass blade dynamics and wave attenuation based on numerical and laboratory experiments. Limnol. Oceanogr. 59, 251–266. https://doi.org/10.4319/lo.2014.59.1.0251.

Zhang, X., Nepf, H., 2024. Laboratory data linking the reconfiguration of and drag on individual plants to the velocity structure and wave dissipation over a meadow of salt marsh plants under waves with and without current. Earth Syst. Sci. Data 16, 1047–1062. https://doi.org/10.5194/essd-16-1047-2024.

Zhang, X., Nepf, H., 2021. Wave damping by flexible marsh plants influenced by current. Phys. Rev. Fluids 6, 100502. https://doi.org/10.1103/PhysRevFluids.6.100502.

Zhu, L., Chen, Q., Ding, Y., Jafari, N., Wang, H., Johnson, B.D., 2022. Towards a unified drag coefficient formula for quantifying wave energy reduction by salt marshes. Coast. Eng., 104256 https://doi.org/10.1016/j.coastaleng.2022.104256.